AIAA Journal
Vol. 54, No. 1, January 2016

Accurate Response of Wing Structures to Free-Vibration, Load Factors, and Nonstructural Masses

Erasmo Carrera* and Alfonso Pagani†
Politecnico di Torino, 10129 Torino, Italy

DOI: 10.2514/1.J054164

Based on the Carrera unified formulation, this work extends variable kinematic finite beam elements to include load factors and nonstructural masses for the static and vibration analyses of complex, metallic wing structures. According to the Carrera unified formulation, variable kinematic beam theories are formulated in an automatic and hierarchical manner by expressing the displacement field as an arbitrary expansion through generic cross-sectional functions. Both Taylor-like and Lagrange polynomials are used in this paper to develop refined beam kinematics, and the related theories are referred to as Taylor expansion and Lagrange expansion, respectively. The generalized unknowns of Taylor expansion models are the beam axis displacements and the *N*-order displacement derivatives, with *N* being a free parameter of the analysis. Classical beam theories are clearly particular cases of the linear ($N = 1$) Taylor expansion model. On the other hand, Lagrange expansion models have only pure translational displacements as unknowns. By exploiting this characteristic of Lagrange expansion, a componentwise approach is implemented and used for the analysis of multicomponent reinforced-shell structures. Numerical applications are developed by classical finite element procedures, and both static response and free vibration analyses are addressed. Various configurations of a benchmark wing are considered, and the capabilities of the present methodologies when dealing with higher-order effects due to deformable cross sections and geometrical discontinuities (for example, underside windows) are evaluated. The attention is focused on the applicability of the present refined beam models to problems involving complex, external inertial loadings. The results are compared to finite element solutions from commercial tools, including full three-dimensional models and models obtained by assembling two-dimensional shell and one-dimensional finite elements.

Nomenclature

E	=	elastic modulus
F_τ	=	cross-section functions
G	=	shear modulus
$\mathbf{K}^{ij\tau s}$	=	fundamental nucleus of the elemental stiffness matrix
L_{ext}	=	work of external loadings
L_{ine}	=	work of inertial loadings
L_{int}	=	strain energy
l	=	dimension of the structure in the y direction
M	=	number of expansion terms
$\mathbf{M}^{ij\tau s}$	=	fundamental nucleus of the elemental mass matrix
$\tilde{m}$	=	nonstructural mass
N	=	expansion order for Taylor expansion models
N_i	=	one-dimensional shape functions
$\boldsymbol{P}$	=	applied point load
P_x, P_y, P_z	=	three-dimensional loading components
$\boldsymbol{P}_{\text{ine}}^{i\tau}$	=	fundamental nucleus of the load due to acceleration fields
p	=	polynomial order of the shape functions
$\boldsymbol{q}$	=	vector of the nodal generalized displacements
r, s	=	natural coordinates
$\mathsf{r}_\tau, \mathsf{s}_\tau$	=	natural coordinates of the Lagrange points
$\boldsymbol{u}$	=	three-dimensional displacements vector
$\boldsymbol{u}_\tau$	=	generalized displacements vector
u_x, u_y, u_z	=	three-dimensional displacement components
$u_{x1}, u_{y1}, u_{z1}, u_{x2}, \ldots, u_{zM}$	=	generalized displacement components
$\ddot{\boldsymbol{u}}_0$	=	applied three-dimensional acceleration field
$\ddot{u}_{x_0}, \ddot{u}_{y_0}, \ddot{u}_{z_0}$	=	components of the applied acceleration field
V	=	beam volume; $\Omega \times L$
(x, y, z)	=	coordinates reference system
(x_m, y_m, z_m)	=	application point of the nonstructural mass
(x_p, y_p, z_p)	=	application point of the concentrated load
δ	=	virtual variation
$\boldsymbol{\epsilon}$	=	strain vector
ν	=	Poisson ratio
λ	=	Lame's parameter
ρ	=	material density
$\boldsymbol{\sigma}$	=	stress vector
Ω	=	cross-section domain

I. Introduction

In ENGINEERING practice, problems involving load factors and nonstructural masses are of particular interest [1]. A notable example is that of aerospace engineering. In aerospace design, for instance, nonstructural masses are used in finite element (FE) models to incorporate the weight of the engines, fuel, and payload. On the other hand, the most critical points in the aircraft and spacecraft mission profiles are usually prescribed in terms of load factors. Thus, the importance of having accurate models able to take into account those inertial effects is evident. This aspect is also confirmed by the rich literature on the argument. In [2], for example, structural

Received 21 January 2015; revision received 9 July 2015; accepted for publication 20 July 2015; published online 6 October 2015.

*Professor of Aerospace Structures and Aeroelasticity, Department of Mechanical and Aerospace Engineering, Corso Duca degli Abruzzi 24; erasmo.carrera@polito.it. Member AIAA.

†Research Fellow, Department of Mechanical and Aerospace Engineering, Corso Duca degli Abruzzi 24; alfonso.pagani@polito.it.

vibrations of slender missile containing many nonstructural masses were carried out by using the method of equivalent density and shell FEs. Ghosh and Ghanem [3] performed random eigenvalue analysis of a Goland wing, considering the nonstructural masses attached to the wing as a source of uncertainty. Shenyan [4] demonstrated the importance of inertial effects on structural analyses and optimal designs. Nikkhoo et al. [5] carried out the vibration analysis of a thin rectangular plate due to multiple travelling inertial loads. In the present paper, accurate and efficient one-dimensional (1-D) higher-order models able to take into account the effects due to localized inertia and load factors in structural analyses of complex wing structures are proposed and assessed.

Aircraft structures are reinforced thin shells. These are also called semimonocoque constructions, which are obtained by assembling three main components: skins (or panels), longitudinal stiffening members (including spar caps and stringers), and transversal stiffeners (ribs). A brief overview of the evolution and the state of the art of modeling techniques for reinforced-shell structures is given hereafter.

A number of different approaches were developed in the first half of the last century. These are discussed in major reference books [6,7]. Among these approaches, the so-called pure semimonocoque (or "idealized semimonocoque") is the most popular, and it assumes constant shear into panels and webs. The main advantage of this approach is that it leads to a system of linear algebraical equations in the case of static response analysis. However, the number of such equations increases for structures with high redundancies and multibay box wings. The number of resulting equations (and redundancies) can be strongly reduced by coupling the pure semimonocoque approach with the assumptions from classical beam theories, such as the Euler–Bernoulli beam model (EBBM) or Timoshenko beam model (TBM).

Due to the advent of computational methods [mostly the finite element method (FEM)] and to the demand for more accuracy, the analysis of complex aircraft structures continued to be made using a combination of solid [three-dimensional (3-D)], plate/shell [two-dimensional (2-D)], and beam (1-D) models. The possible manner in which stringers, spar caps, spar webs, panels, and ribs are introduced into FE mathematical models is part of the knowledge of structural analysts; in general, the coupling of elements with different dimensionality is not trivial. Several works have shown, in fact, the necessity for a proper simulation of the stiffeners-panel "linkage." For example, Satsangi and Mukhopadhyay [8] used eight-node plate elements, assuming the same displacement field for stiffeners and plates. Kolli and Chandrashekhara [9] formulated an FE model with a nine-node plate and three-node beam elements. Prusty [10] carried out linear static analyses of composite laminated shells using a combination of eight-node plate elements and three-node beam elements. With regard to vibration analysis of reinforced-shell structures, which is also one of the topics of the present work, Samanta and Mukhopadhyay [11] developed a new stiffened shell element; subsequently, they used their formulation to determine natural frequencies and mode shapes of different stiffened structures. Bouabdallah and Batoz [12] presented a finite element model for the static and free vibration analysis of composite cylindrical panels with composite stiffeners. In [13], Thinh and Khoa developed a nine-node stiffened plate element for the modal analysis of laminated stiffened plates with arbitrary oriented stiffeners based on Mindlin's deformation plate theory. Recently, Vörös [14] formulated a new plate/shell stiffener element. In Vörös's theory, the reinforcement was developed by employing a general beam theory, including the constraint torsional warping effect and the second-order terms of finite rotations.

The works mentioned so far show a definite interest in investigating FEM applications to reinforced-shell structures including inertial effects. However, in most of the papers in the literature, such as some of those cited previously, plates/shells and stiffeners are modeled separately, and a simulation of the stiffener panel is often required. Usually, the nodes of the beam elements are connected to those of the shell elements via rigid fictitious links. This technique presents some discrepancies. The principal problems, however, are that the out-of-plane warping displacements in the stiffener section are neglected, and the beam torsional rigidity is not correctly predicted. To overcome those issues, Patel et al. [15] introduced a torsion correction factor. In Vörös's works [14,16], the connection between the plate/shell and the stiffener was modeled through a special transformation, which included torsional–bending coupling and the eccentricity of internal forces between the stiffener and the plate elements. Conversely, the formulation used in the present paper deals with reinforced shells using a refined 1-D formulation, with no need to introduce "fictitious links" to connect beam and shell elements. This approach is denoted to as componentwise (CW), and it merely makes use of the physical surfaces of the structures to build a mathematical model. Nowadays, this same result is achievable only by employing 3-D solid FE elements.

CW falls within the framework of the Carrera unified formulation (CUF); see [17]. The CUF is a hierarchical methodology that enables one to develop higher-order theories automatically, without the need for ad hoc assumptions. According to the CUF, in fact, the displacement field is the expansion of generic functions on the beam cross section. Depending on the choice of those functions, multiple classes of theories of structures can be formulated. For example, in the case of beam models [18], the Taylor expansion (TE) class makes use of Taylor-like polynomials to enrich 1-D kinematics, and it has been validated in various papers in the literature for both static and free vibration analyses (see, for example, [19]). On the other hand, Lagrange polynomials are used to discretize the displacement field on the cross section in Lagrange expansion (LE) CUF beam models, and they are employed in this work to implement CW models of complex wing structures.

In the present paper, the CUF is used to formulate and compare various FE beam models (including classical ones, as well as refined TE and CW ones) of reinforced-shell structures. The attention is focused on the capabilities of these beam theories to deal with both static and free vibrations analyses, as well as with complex loading conditions due to load factors and nonstructural masses, which have been recently introduced and tested in the framework of the CUF in [20–22].

The paper is organized as follows:

1) First, the CUF is introduced and variable kinematic beam theories based on TE are developed.

2) The LE formulation and the related CW approach are then presented.

3) Next, FE arrays, including load vectors due to arbitrary inertial fields, are formulated and expressed in terms of fundamental nuclei, which do not depend on the theory type and order.

4) Subsequently, various configurations of a benchmark metallic wing are considered and the numerical results are discussed.

5) The main conclusions are finally outlined.

II. Carrera Unified Formulation

A. Classical Beam Theories and Refined Kinematics by TE

Figure 1 shows the rectangular Cartesian coordinate system and the geometry of the benchmark wing discussed in this work. In the case of simple, preliminary analyses (and if sufficiently long), the wing might be modeled by the EBBM with acceptable accuracy; the kinematic field of the EBBM can be written as

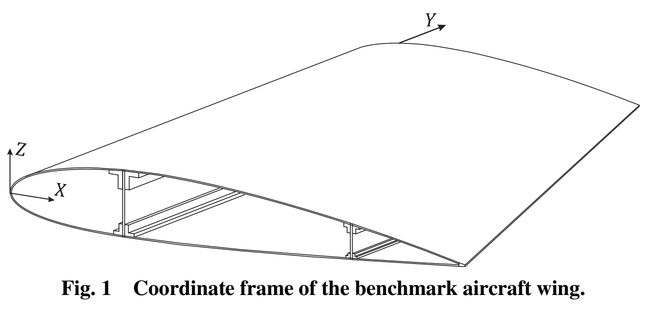

Fig. 1 Coordinate frame of the benchmark aircraft wing.

$$u_x = u_{x1}$$
$$u_y = u_{y1} - x\frac{\partial u_{x1}}{\partial y} + z\frac{\partial u_{z1}}{\partial y}$$
$$u_z = u_{z1} \tag{1}$$

where u_x, u_y, and u_z are the displacement components of a point belonging to the beam domain along x, y, and z, respectively; u_{x1}, u_{y1}, and u_{z1} are the displacements of the beam axis; $-(\partial u_{x1}/\partial y)$ and $\partial u_{z1}/\partial y$ are the rotations of the cross section about the z axis (i.e., ϕ_z) and x axis (i.e., ϕ_x). According to the EBBM, the deformed cross section remains plane and orthogonal to the beam axis because cross-sectional shear deformation phenomena are neglected. Shear stresses play a significant role in several problems (e.g., short beams, composite structures), and their neglect can lead to incorrect results. One may want to generalize Eq. (1) and overcome the EBBM assumption of the orthogonality of the cross section. The improved displacement field results in the TBM:

$$u_x = u_{x1}$$
$$u_y = u_{y1} + x\phi_z + z\phi_x$$
$$u_z = u_{z1} \tag{2}$$

The TBM constitutes an improvement over the EBBM because the cross section does not necessarily remain perpendicular to the beam axis after deformation, and two degrees of freedom (i.e., the unknown rotations ϕ_z and ϕ_x) are added to the original displacement field.

Classical beam models grant reasonably good results when slender solid-section homogeneous structures undergo bending. On the other hand, the analysis of short thin-walled open cross-section beams may require more sophisticated theories to achieve sufficiently accurate results; see [23]. Many refined beam theories have been proposed over the last century to overcome the limitations of classical beam modeling (e.g., nonfulfillment of homogeneous condition of the transverse stress components at lateral surfaces of the beam); see [19,24,25] for a comprehensive review of beam theories. However, as a general guideline, one can state that, the richer the kinematic field, the more accurate the 1-D model becomes [26]. For example, one can demonstrate that a linear distribution of transverse displacement components (i.e., u_x and u_z) is needed to detect the rigid rotation of the cross section about the beam axis. Conversely, a third-order displacement field (see [27,28]) can be adopted to overcome the inconsistency of the TBM and fulfill the homogeneous condition of shear stresses on the lateral surfaces. However, richer displacement fields lead to a higher amount of equations to solve; moreover, the choice of the additional expansion terms is generally problem dependent.

The Carrera unified formulation can be considered like a tool for tackling the problem of the choice of the expansion terms. Let $\boldsymbol{u} = \{u_x \quad u_y \quad u_z\}^T$ be the transposed displacement vector. According to the CUF, a generic displacement field can be expressed in a compact fashion as an N-order expansion in terms of generic functions F_τ:

$$\boldsymbol{u}(x,y,z) = F_\tau(x,z)\boldsymbol{u}_\tau(y), \qquad \tau = 1,2,\ldots,M \tag{3}$$

where F_τ are the functions of the coordinates x and z on the cross section; $\boldsymbol{u}_\tau$ is the vector of the generalized displacements; and M stands for the number of terms used in the expansion. Taylor expansion CUF models use MacLaurin expansions as F_τ; i.e., 2-D polynomials $x^i z^j$ (i and j are positive integers) are exploited as basis functions to generate beam theories. It should be noted that Eqs. (1) and (2) are particular cases of the linear ($N = 1$) TE model, which can be expressed as

$$u_x = u_{x_1} + xu_{x_2} + zu_{x_3}$$
$$u_y = u_{y_1} + xu_{y_2} + zu_{y_3}$$
$$u_z = u_{z_1} + xu_{z_2} + zu_{z_3} \tag{4}$$

where the parameters on the right-hand side ($u_{x_1}, u_{y_1}, u_{z_1}, u_{x_2}$, etc.) are the displacements of the beam axis and their first derivatives. Higher-order terms can be taken into account according to Eq. (3). For instance, it is clear that the displacement field of the third-order Heyliger and Reddy model [28] can be considered as a particular case of the $N = 3$ TE model; i.e.,

$$u_x = u_{x_1} + xu_{x_2} + zu_{x_3} + x^2u_{x_4} + xzu_{x_5} + z^2u_{x_6} + x^3u_{x_7} + x^2zu_{x_8} + xz^2u_{x_9} + z^3u_{x_{10}}$$
$$u_y = u_{y_1} + xu_{y_2} + zu_{y_3} + x^2u_{y_4} + xzu_{y_5} + z^2u_{y_6} + x^3u_{y_7} + x^2zu_{y_8} + xz^2u_{y_9} + z^3u_{y_{10}}$$
$$u_z = u_{z_1} + xu_{z_2} + zu_{z_3} + x^2u_{z_4} + xzu_{z_5} + z^2u_{z_6} + x^3u_{z_7} + x^2zu_{z_8} + xz^2u_{z_9} + z^3u_{z_{10}} \tag{5}$$

The possibility of dealing with arbitrary expansion makes the TE CUF models able to handle complex problems, such as thin-walled structures and local effects.

B. Lagrange Expansion Models and Componentwise Approach

The degrees of freedom of the TE models described previously (i.e., displacements and N-order derivatives of displacements) are defined along the axis of the beam. The unknown variables are only pure displacements if Lagrange polynomials are adopted as expanding functions F_τ in Eq. (3). The resulting models are referred to as Lagrange expansion, and they were first introduced in [29]. Recently, LE beam theory has been used for the componentwise modeling of complex structures, namely, aerospace [30,31] and civil engineering [32] structures. The term CW refers to the fact that Lagrange elements are used to model the displacement variables in each structural component at the cross-sectional level.

In this work, three types of cross-sectional Lagrange polynomial sets were adopted to build CW models, and they are shown in Fig. 2.

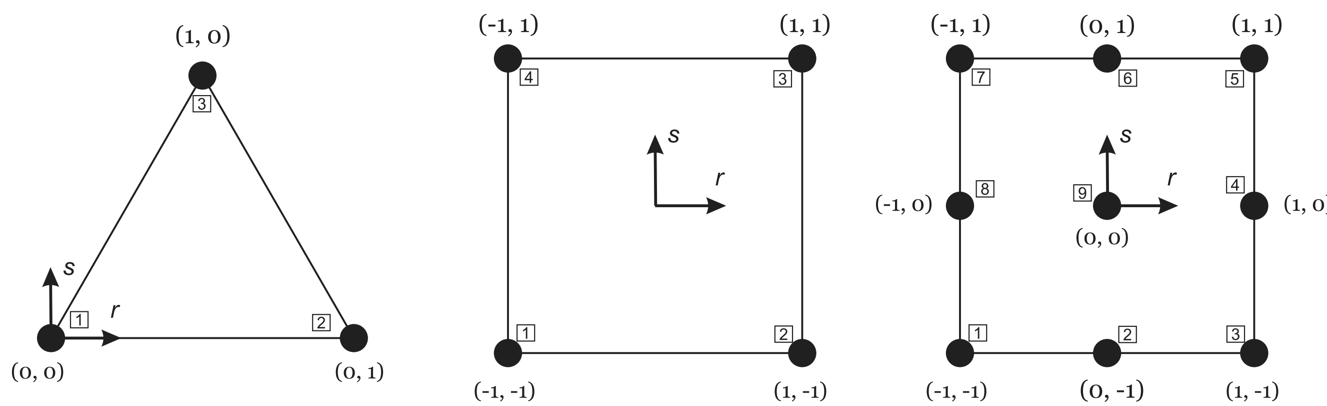

Fig. 2 Cross-section L elements in natural geometry.

In particular, three-point linear (L3), four-point bilinear (L4), and nine-point biquadratic (L9) polynomials were used. The isoparametric formulation was exploited to deal with arbitrary shaped geometries. The Lagrange polynomials can be found in [33]. However, the interpolation functions in the case of the L9 element are given as an example:

$$F_\tau = \frac{1}{4}(\mathsf{r}^2 + \mathsf{r}\mathsf{r}_\tau)(\mathsf{s}^2 + \mathsf{s}\mathsf{s}_\tau) \qquad \tau = 1,3,5,7$$
$$F_\tau = \frac{1}{2}\mathsf{s}_\tau^2(\mathsf{s}^2 - \mathsf{s}\mathsf{s}_\tau)(1-\mathsf{r}^2) + \frac{1}{2}\mathsf{r}_\tau^2(\mathsf{r}^2 - \mathsf{r}\mathsf{r}_\tau)(1-\mathsf{s}^2) \qquad \tau = 2,4,6,8$$
$$F_\tau = (1-\mathsf{r}^2)(1-\mathsf{s}^2) \qquad \tau = 9 \tag{6}$$

where r and s vary from -1 to $+1$, whereas r_τ and s_τ are the coordinates of the nine points for which the numbering and location in the natural coordinate frame are summarized in Fig. 2c. The displacement field given by an L9 element is therefore

$$u_x = F_1 u_{x_1} + F_2 u_{x_2} + \ldots + F_9 u_{x_9}$$
$$u_y = F_1 u_{y_1} + F_2 u_{y_2} + \ldots + F_9 u_{y_9}$$
$$u_z = F_1 u_{z_1} + F_2 u_{z_2} + \ldots + F_9 u_{z_9} \tag{7}$$

where $u_{x_1}, \ldots, u_{z_9}$ are the displacement variables of the problem, and they represent the translational displacement components of each of the nine points of the L9 element. For further refinements, the cross section can be discretized by using several L elements as in Fig. 3, where two assembled L9 elements are shown; this is one of the most important characteristics of the CW approach.

Most of the engineering structures are made of different components, such as spar caps, stringers, longerons, ribs, and panels in the case of aerospace constructions. However, these components usually have different geometries and scales. Through the CW approach, one can model each typical part of a structure through the 1-D CUF LE formulation. In a finite element framework, this means that different components are modeled by means of the same 1-D finite element. An example of CW modeling of a typical wing is shown in Fig. 4. According to the CW technique, each component of the structure is modeled via beam elements. Then, by exploiting the natural capability of LE to be assembled on the cross section, Lagrange polynomials (L9 in Fig. 4) are appropriately used to arbitrary refine the beam kinematics. Compatibilities between the various components are enforced in terms of displacements by superimposing cross-sectional nodes. Alternatively, mathematical techniques might be used; see [34,35]. If a rib were present in the wing in Fig. 4, it would be modeled by beam elements laying on the longitudinal axis; see [30]. One of the main features of the CW methodology is that it allows for tuning the capabilities of the model by 1) choosing which component requires a more detailed model; and 2) setting the order of the structural model to be used. Higher-order phenomena (i.e., warping and 3-D strain effects) can be, in fact, automatically described by the CUF models by opportunely enriching the beam kinematics (see [17,30]). Moreover, via the CW approach, FE mathematical models can be built by using only physical boundaries; artificial lines (beam axes) and surfaces (plate/shell reference surfaces) are no longer necessary.

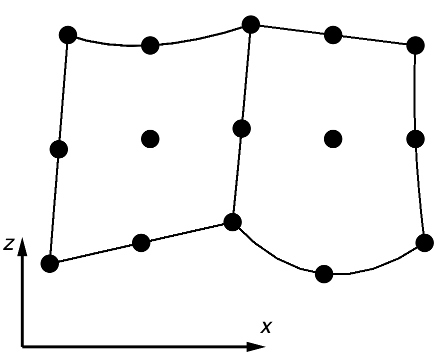

Fig. 3 Two assembled L9 elements in actual geometry.

III. Finite Element Approximation

A. Fundamental Nuclei

The FE approach is adopted to discretize the structure along the y axis (i.e., the longitudinal axis in Fig. 1). This process is accomplished via a classical finite element technique, where the displacement vector is given by

$$\boldsymbol{u}(x,y,z) = F_\tau(x,z) N_i(y) \boldsymbol{q}_{\tau i}, \qquad \tau = 1,\ldots,M,\ i = 1,\ldots,p+1 \tag{8}$$

N_i stands for the shape functions of order p, and $\boldsymbol{q}_{\tau i}$ is the nodal displacement vector:

$$\boldsymbol{q}_{\tau i} = \{ q_{u_{x_{\tau i}}} \quad q_{u_{y_{\tau i}}} \quad q_{u_{z_{\tau i}}} \}^T \tag{9}$$

The shape functions are not given here. They can be found in many books; see, for example, [36]. Elements with four nodes (B4) were adopted in this work, i.e., a cubic approximation ($p = 3$) along the y axis was assumed. The cross-section discretization for the LE class (i.e., the choice of the type, the number, and the distribution of cross-sectional Lagrange elements), or of the theory order N for the TE class, are entirely independent of the choice of the beam finite element to be used along the axis of the beam.

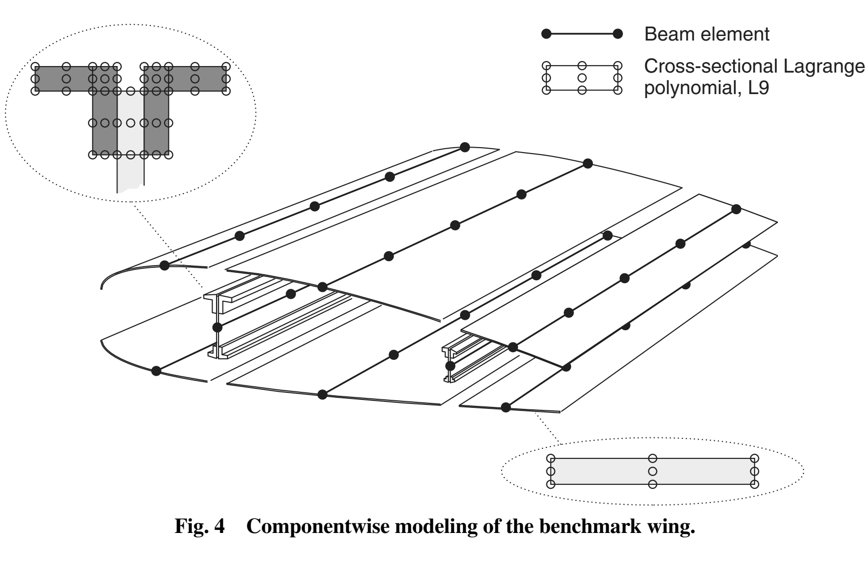

Fig. 4 Componentwise modeling of the benchmark wing.

The stiffness and mass matrices, as well as the loading vector of the elements, are obtained via the principle of virtual displacements, which in its general form holds

$$\delta L_{\text{int}} = \int_V \delta \boldsymbol{\epsilon}^T \boldsymbol{\sigma}\, \mathrm{d}V = \delta L_{\text{ext}} - \delta L_{\text{ine}} \tag{10}$$

where L_{int} stands for the strain energy; L_{ext} is the work of the external loads; L_{ine} is the work of the inertial loadings; δ stands for the virtual variation; $V = \Omega \times l$ is the volume of the beam, with Ω being the cross-section area and $l$is the length of the structure; and $\boldsymbol{\epsilon}$ and $\boldsymbol{\sigma}$ are the strain and stress vectors, respectively. The virtual variation of the strain energy is rewritten using the constitutive laws, the linear strain-displacement relations, and Eq. (8). It reads

$$\delta L_{\text{int}} = \delta \boldsymbol{q}_{\tau i}^T \mathbf{K}^{ij\tau s} \boldsymbol{q}_{sj} \tag{11}$$

where $\mathbf{K}^{ij\tau s}$ is the stiffness matrix in the form of the fundamental nucleus. The derivation of the FE fundamental nucleus of the stiffness matrix is not repeated here for the sake of brevity, but it is given in [17], where more details about the CUF can also be found. However, the components of the stiffness matrix nucleus are provided in the following, and they are referred to as $\mathbf{K}_{rc}^{ij\tau s}$, where r is the row number ($r = 1, 2, 3$) and c is the column number ($c = 1, 2, 3$):

$$\begin{aligned}
\mathbf{K}_{11}^{ij\tau s} &= (\lambda + 2G) \int_\Omega F_{\tau,_x} F_{s,_x}\, \mathrm{d}\Omega \int_l N_i N_j\, \mathrm{d}y \\
&+ G \int_\Omega F_{\tau,_z} F_{s,_z}\, \mathrm{d}\Omega \int_l N_i N_j\, \mathrm{d}y + G \int_\Omega F_\tau F_s\, \mathrm{d}\Omega \int_l N_{i,_y} N_{j,_y}\, \mathrm{d}y \\
\mathbf{K}_{12}^{ij\tau s} &= \lambda \int_\Omega F_{\tau,_x} F_s\, \mathrm{d}\Omega \int_l N_i N_{j,_y}\, \mathrm{d}y + G \int_\Omega F_\tau F_{s,_x}\, \mathrm{d}\Omega \int_l N_{i,_y} N_j\, \mathrm{d}y \\
\mathbf{K}_{13}^{ij\tau s} &= \lambda \int_\Omega F_{\tau,_x} F_{s,_z}\, \mathrm{d}\Omega \int_l N_i N_j\, \mathrm{d}y + G \int_\Omega F_{\tau,_z} F_{s,_x}\, \mathrm{d}\Omega \int_l N_i N_j\, \mathrm{d}y \\
\mathbf{K}_{21}^{ij\tau s} &= \lambda \int_\Omega F_\tau F_{s,_x}\, \mathrm{d}\Omega \int_l N_{i,_y} N_j\, \mathrm{d}y + G \int_\Omega F_{\tau,_x} F_s\, \mathrm{d}\Omega \int_l N_i N_{j,_y}\, \mathrm{d}y \\
\mathbf{K}_{22}^{ij\tau s} &= G \int_\Omega F_{\tau,_z} F_{s,_z}\, \mathrm{d}\Omega \int_l N_i N_j\, \mathrm{d}y + G \int_\Omega F_{\tau,_x} F_{s,_x}\, \mathrm{d}\Omega \int_l N_i N_j\, \mathrm{d}y \\
&+ (\lambda + 2G) \int_\Omega F_\tau F_s\, \mathrm{d}\Omega \int_l N_{i,_y} N_{j,_y}\, \mathrm{d}y \\
\mathbf{K}_{23}^{ij\tau s} &= \lambda \int_\Omega F_\tau F_{s,_z}\, \mathrm{d}\Omega \int_l N_{i,_y} N_j\, \mathrm{d}y + G \int_\Omega F_{\tau,_z} F_s\, \mathrm{d}\Omega \int_l N_i N_{j,_y}\, \mathrm{d}y \\
\mathbf{K}_{31}^{ij\tau s} &= \lambda \int_\Omega F_{\tau,_z} F_{s,_x}\, \mathrm{d}\Omega \int_l N_i N_j\, \mathrm{d}y + G \int_\Omega F_{\tau,_x} F_{s,_z}\, \mathrm{d}\Omega \int_l N_i N_j\, \mathrm{d}y \\
\mathbf{K}_{32}^{ij\tau s} &= \lambda \int_\Omega F_{\tau,_z} F_s\, \mathrm{d}\Omega \int_l N_i N_{j,_y}\, \mathrm{d}y + G \int_\Omega F_\tau F_{s,_z}\, \mathrm{d}\Omega \int_l N_{i,_y} N_j\, \mathrm{d}y \\
\mathbf{K}_{33}^{ij\tau s} &= (\lambda + 2G) \int_\Omega F_{\tau,_z} F_{s,_z}\, \mathrm{d}\Omega \int_l N_i N_j\, \mathrm{d}y \\
&+ G \int_\Omega F_{\tau,_x} F_{s,_x}\, \mathrm{d}\Omega \int_l N_i N_j\, \mathrm{d}y + G \int_\Omega F_\tau F_s\, \mathrm{d}\Omega \int_l N_{i,_y} N_{j,_y}\, \mathrm{d}y
\end{aligned} \tag{12}$$

where G and λ are the Lamé parameters. If Poisson ν and Young E moduli are used, one has

$$G = \frac{E}{2(1+\nu)}$$

and

$$\lambda = \frac{\nu E}{(1+\nu)(1-2\nu)}$$

The fundamental nucleus has to be expanded according to the summation indexes τ and s in order to obtain the elemental stiffness matrix.

The virtual variation of the work of the inertial loadings is

$$\delta L_{\text{ine}} = \int_V \rho \delta \boldsymbol{u}^T \ddot{\boldsymbol{u}}\, \mathrm{d}V \tag{13}$$

where ρ stands for the density of the material, and $\ddot{\boldsymbol{u}}$ is the acceleration vector. Equation (13) is rewritten using Eq. (8):

$$\delta L_{\text{ine}} = \delta \boldsymbol{q}_{\tau i}^T \int_l N_i N_j\, \mathrm{d}y \int_\Omega \rho F_\tau F_s\, \mathrm{d}\Omega \ddot{\boldsymbol{q}}_{sj} = \delta \boldsymbol{q}_{\tau i}^T \mathbf{M}^{ij\tau s} \ddot{\boldsymbol{q}}_{sj} \tag{14}$$

where $\mathbf{M}^{ij\tau s}$ is the fundamental nucleus of the mass matrix. Its components are provided in the following, and they are referred to as $\mathbf{M}_{rc}^{ij\tau s}$, where r is the row number ($r = 1, 2, 3$) and c denotes column number ($c = 1, 2, 3$):

$$\begin{aligned}
\mathbf{M}_{11}^{ij\tau s} &= \mathbf{M}_{22}^{ij\tau s} = \mathbf{M}_{33}^{ij\tau s} = \rho \int_l N_i N_j\, \mathrm{d}y \int_\Omega F_\tau F_s\, \mathrm{d}\Omega \\
\mathbf{M}_{12}^{ij\tau s} &= \mathbf{M}_{13}^{ij\tau s} = \mathbf{M}_{21}^{ij\tau s} = \mathbf{M}_{23}^{ij\tau s} = \mathbf{M}_{31}^{ij\tau s} = \mathbf{M}_{32}^{ij\tau s} = 0
\end{aligned} \tag{15}$$

It is noteworthy that no assumptions about the approximation order have been made in formulating $\mathbf{K}^{ij\tau s}$ and $\mathbf{M}^{ij\tau s}$. It is, therefore, possible to obtain refined beam models without changing the formal expression of the nuclei components. This property of the nuclei is the key point of the CUF that allows, with only nine coding statements, the implementation of any order of multiple class theories.

The loadings vector, which is variationally coherent to the model, can be derived with relative ease in the case of a generic concentrated load $\boldsymbol{P}$ acting on the application point (x_p, y_p, z_p):

$$\boldsymbol{P} = \{\, P_x \quad P_y \quad P_z \,\}^T \tag{16}$$

Any other loading condition can be treated similarly. The virtual work due to $\boldsymbol{P}$ is

$$\delta L_{\text{ext}} = \delta \boldsymbol{u}^T \boldsymbol{P} \tag{17}$$

After using Eq. (8), Eq. (17) becomes

$$\delta L_{\text{ext}} = F_\tau N_i \delta \boldsymbol{q}_{\tau i}^T \boldsymbol{P} \tag{18}$$

where F^τ and N_i are evaluated in (x_p, z_p) and y_p, respectively. The last equation allows the identification of the components of the nucleus that have to be loaded; that is, it allows the proper assembling of the loading vector by detecting the displacement variables that have to be loaded. In the next section, the attention is focused on the special cases of load factors and nonstructural masses.

B. Load Factors and Nonstructural Masses in the Framework of CUF Theories

When using classical beam theories, translational as well as rotational load factors are usually applied with respect to the reference axis, or with respect to the shear axis if transverse stresses are also modeled. In this paper, the capability of the present refined beam models to take into account the effects due to 3-D distributions of applied inertial loads is also highlighted. Let the following acceleration field be applied to the structure:

$$\ddot{\boldsymbol{u}}_0(x, y, z) = \{\, \ddot{u}_{x_0} \quad \ddot{u}_{y_0} \quad \ddot{u}_{z_0} \,\}^T \tag{19}$$

The virtual variation of the external work δL_{ext} due to the acceleration field $\ddot{\boldsymbol{u}}_0$ is given by

$$\delta L_{\text{ext}} = \int_V \rho \delta \boldsymbol{u}^T \ddot{\boldsymbol{u}}_0\, \mathrm{d}V \tag{20}$$

Equation (8) is substituted into Eq. (20). It reads

Table 1 Considered load cases

	Point load F_z		Load factor n_z	Localized inertia	
	Magnitude, N	Position	Magnitude, g	Magnitude, kg	Position
Load case 1	−3000	Point 4, $y = \frac{2}{3}l$	— —	— —	— —
Load case 2	— —	— —	1	— —	— —
Load case 3	— —	— —	1	300	Point 4, $y = \frac{1}{3}l$

$$\delta L_{\text{ext}} = \delta \boldsymbol{q}_{\tau i}^T \left[\int_\Omega \rho F_\tau F_s \left(\int_y N_i N_j \, \mathrm{d}y \right) \mathrm{d}\Omega \right] \ddot{\boldsymbol{q}}_{sj_0} \tag{21}$$

where the term between square brackets is the fundamental nucleus of the mass matrix $\mathbf{M}^{ij\tau s}$. The virtual variation of the external work is, therefore, written as

$$\delta L_{\text{ext}} = \delta \boldsymbol{q}_{\tau i}^T \mathbf{M}^{ij\tau s} \ddot{\boldsymbol{q}}_{sj_0} = \delta \boldsymbol{q}_{\tau i}^T \boldsymbol{P}_{\text{ine}}^{i\tau} \tag{22}$$

where $\boldsymbol{P}_{\text{ine}}^{i\tau}$ is the nucleus of the loading vector due to the acceleration field. It is important to underline that arbitrarily 3-D distributed accelerations can be applied for both TE and LE, even though they are beam models.

In the present paper, the effect due to nonstructural masses is also investigated. Localized inertia can, in principle, be arbitrarily placed in the 3-D domain of the beam structure. In the framework of the CUF, this is easily realized by adding the following term to the fundamental nucleus of the mass matrix:

$$\boldsymbol{m}^{ijts} = \boldsymbol{I}[F_\tau(x_m, z_m) F_s(x_m, z_m) N_i(y_m) N_j(y_m)]\tilde{m} \tag{23}$$

where $\boldsymbol{I}$ is the 3×3 identity matrix; and $\tilde{m}$ is the value of the nonstructural mass, which is applied at point (x_m, y_m, z_m).

IV. Numerical Results

The present refined 1-D models have been evaluated by analyzing several configurations of a metallic benchmark wing, which is depicted in Fig. 1. The considered wing is straight with a NACA 2415 airfoil. The chord c is equal to 1 m. The thickness of each panel is 3 mm, whereas the thickness of the spar webs is 5 mm. The cross-sectional dimensions of the spars' caps can be found in [31], together with further details on the benchmark wing. The overall length of the structure is $l = 6$ m. For illustrative purposes, the wing is completely metallic and the adopted material is an aluminum alloy with the following characteristics: elastic modulus $E = 75$ GPa; Poisson ratio $\nu = 0.33$; and density $\rho = 2700$ kg/m^3.

First, the wing configuration with no ribs is assessed. Next, more complex wing structures are discussed to highlight the capabilities of the present beam models to deal with transverse stiffening members and windows. Both TE and CW models of the benchmark wing were developed, and the correspondent results were compared with both classical beam theories and FE models from the commercial codes MSC Nastran and Abaqus. Regarding those FEM models used for comparisons, both full 3-D models and models obtained by combining 2-D shell and 1-D beam elements have been considered. Although, the 3-D elasticity models have been mainly used for comparing static analyses results because of their capabilities to detect complex strain/stress fields. The solid FEM models were obtained by using eight-node CHEXA Nastran elements. On the other hand, the shell/beam model was obtained by using S4R (four-node shell element with reduced integration) shell elements for the panels and spars webs and B31 (two-node linear beam element) beam elements for the spars caps. The sizes of the finite elements for both the Nastran and Abaqus FE models were derived from convergence analyses. Similarly, eight B4 and nine B4 elements were, respectively, used along the beam axis in the cases of CW and TE models, which ensured convergent results. In the case of the ribbed configuration, one B4 element for each rib was added.

In the analyses discussed in the following sections, the attention is particularly focused on the enhanced capability of the present CW models to efficiently deal with complex reinforced structures undergoing inertial loadings, including load factors and localized nonstructural masses, both in the case of static response and vibration analyses.

A. Static Response Analyses

Static analysis of the rib-free configuration of the wings is discussed first. Various load cases are considered, and they are summarized in Table 1. The first load case consists of a point load of $F_z = -3000$ N placed at point 4 (see Fig. 5) at $y = \frac{2}{3}l$. For the load case under consideration, the third to fifth columns of Table 2 quote the vertical displacement u_z measured at point 2 on the cross section at the free edge and the stress components σ_{yy} and σ_{yz}, respectively, at point 3 on the clamped end and at point 5 on the midspan cross section. The results from the present higher-order beam formulations based on both TE and LE are shown in Table 2 and compared to the 3-D solid model by MSC Nastran. Solutions from classical theories (EBBM and TBM) are also given, and they are retrieved as particular cases of the linear ($N = 1$) TE model. Regarding refined TE models, second- ($N = 2$) to eighth-order ($N = 8$) approximations are quoted in the table. The CW model used for the proposed analysis was built by using a combination of L9 elements on the wing cross section, as outlined in [31]. The number of the degrees of freedom (DOFs) is also given in Table 2 for each model implemented. Figure 6 shows the tip cross-section deformation of the wing by different models for the load case under consideration. Furthermore, Fig. 7 shows the distributions of the shear-stress component σ_{yz} by the TBM, the higher-order TE model, CW, and the MSC Nastran solid solutions. In particular, Fig. 7a shows the trend of the transverse stress through the spanwise direction (y axis) in correspondence of point 5 (see Fig. 5). Moreover, the distribution of σ_{yz} along the main spar at the midspan cross section is depicted in Fig. 7b. Finally, Fig. 8 shows the spanwise distribution of the axial stress component σ_{yy} measured at the four spar caps.

In a second load case (see Table 1), the wing underwent a uniform load factor directed to the positive direction of the z axis. The magnitude of the acceleration field was equal to $1g$, with "g" being the gravity acceleration. Results in terms of displacements and stress components, which are measured at the same points as in the previous load case, are given in the sixth to eighth columns in Table 2. Figure 9 shows the deformation of the tip cross section by the EBBM, the seventh-order ($N = 7$) TE model, the CW model, and the MSC Nastran 3-D model. It is clear that, even for load case 2, the wing with no rib is still subjected to differential bending deformation.

To further underline the 3-D capabilities of the present beam formulation, a nonstructural mass was applied at point 5 at $y = \frac{1}{3}l$ for load case 3 (see Table 1). The weight of the mass was equal to 300 kg, and the same load factor as in load case 2 was enforced. A comparison in terms of displacement and stress components between CW, TE-based, and MSC Nastran models is shown in the last columns of Table 2. Finally, Fig. 10 displays the distribution of σ_{yz} along the y axis for the wing with localized inertia subjected to the unitary load factor. The results of the static analyses of the wing without the ribs underline the following:

1) Lower- and higher-order models based on TE, as well as classical beam models, can be locally accurate in terms of

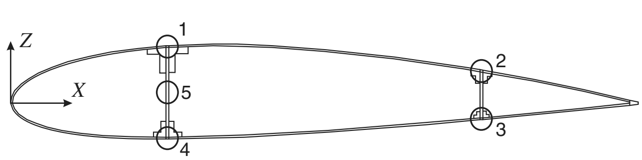

Fig. 5 Notable points on the wing cross section.

Table 2 Selected values of u_z, σ_{yy}, and σ_{yz} for various load cases; wing with no ribs

		Load case 1			Load case 2			Load case 3		
Models	DOFs	u_z[a] mm	σ_{yy}[b] MPa	σ_{yz}[c] MPa	u_z[a] mm	σ_{yy}[b] MPa	σ_{yz}[c] MPa	u_z[a] mm	σ_{yy}[b] MPa	σ_{yz}[c] MPa
					Classical models					
EBBM	84	−57.519	−6.648	— —	21.572	2.574	— —	37.666	5.835	— —
TBM	140	−57.563	−6.647	−0.314	21.590	2.574	0.074	37.705	5.835	0.081
					Higher-order models based on TE					
$N = 2$	504	−55.664	−6.988	−0.339	20.982	2.916	0.058	36.561	7.382	0.064
$N = 4$	1,260	−56.401	−4.705	−2.099	21.273	2.066	0.525	37.176	5.571	0.551
$N = 5$	1,764	−56.553	−5.308	−2.391	21.355	2.304	0.574	37.416	6.194	0.670
$N = 6$	2,352	−56.610	−5.754	−2.470	21.386	2.524	0.595	37.494	6.869	0.760
$N = 7$	3,024	−56.707	−6.881	−2.848	21.429	2.988	0.726	37.592	7.994	0.898
$N = 8$	3,780	−56.731	−6.807	−2.908	21.443	2.908	0.739	37.628	7.580	0.903
					Higher-order model based on LE					
CW	22,200	−56.462	−16.999	−3.182	21.620	7.932	0.638	37.272	15.360	0.317
					MSC Nastran model					
Solid	186,921	−56.671	−14.185	−3.355	21.818	8.153	0.614	37.657	15.461	0.222

[a]u_z at point 2, $y = l$.
[b]σ_{yy} at point 3, $y = 0$.
[c]σ_{yz} at point 5, $y = l/2$.

displacement and axial stress components (e.g., in the close proximity of the top cap of the main spar). However, those models are not able to correctly describe the overall static response of the wing structure, especially if nonsymmetrical loadings are applied and cross-sectional strains/stresses are involved. It is, in fact, clear that, even in the simple case of axial stress analysis, TE-based CUF models produce some errors that increase close to the clamped section.

2) TE-based models, including the EBBM and TBM, are inadequate for detecting transverse shear-stress components in spar webs; in particular, the TBM underestimates shear because it is not able to foresee torsion and differential bending. In the case of refined TE models, the accuracy is slightly increased in terms of shear stresses as the theory order N increases.

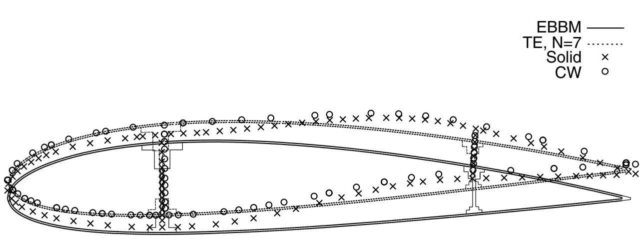

Fig. 6 Tip cross-section deformation under load case 1; wing with no ribs.

3) According to the 3-D reference solution, the CW model is perfectly able to foresee the mechanical behavior of the wing in terms of both displacements and the stress field, even if severe differential bending due to nonsymmetrical loads (e.g., localized inertia) is involved.

4) The computational efforts demanded by the 1-D CW model are significantly lower than those required by the solid Nastran model.

Effects due to ribs on the predictive capabilities of the proposed 1-D methods for static analysis under inertial loads were also examined. Three ribs with a thickness of 6 mm each were, therefore, applied to sections $y = 2$, 4, and 6 m. Additional details about the modeling of the three-bay wing structure and, in particular, the CW modeling of the rib, can be found in [31]. In the proposed analyses, the three-bay wing underwent a uniform load factor ($n_z = 1g$) directed to the positive verse of the z axis (i.e., load case 2 in Table 1). The results are shown in the second to fifth columns of Table 3. Both displacement and stress components are given along with the number of DOFs for each model implemented. The measurement points were the same as in the previous analyses. The spanwise distributions of the axial stress components at the spar caps of the three-bay wing are depicted in Fig. 11. On the other hand, Fig. 12 shows the tip cross-section deformation for the case under consideration. The following comments stem from the analysis of the three-bay benchmark wing:

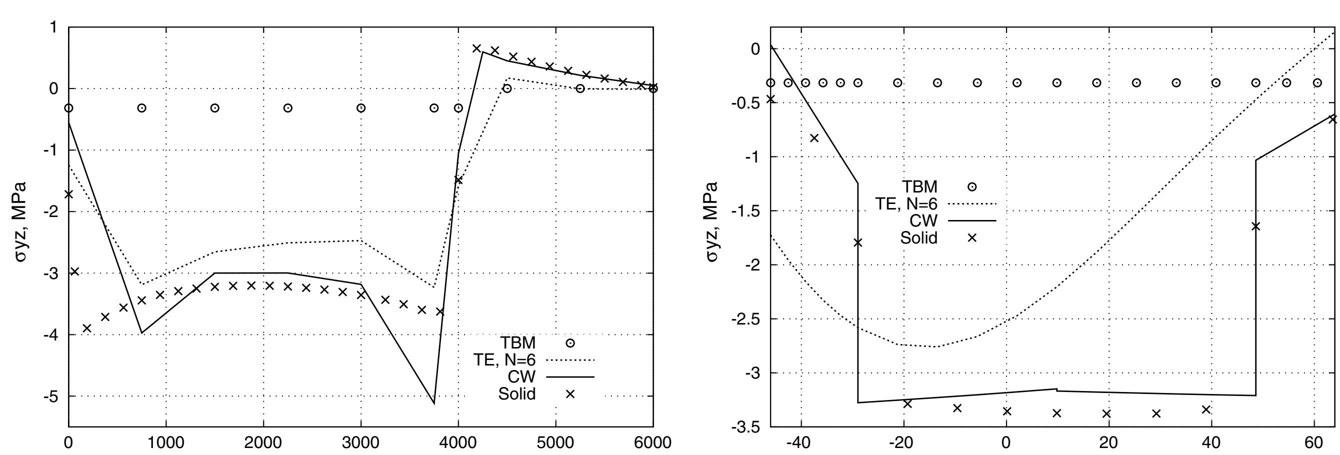

a) σ_{yz} spanwise distribution at point 5 **b) σ_{yz} along the main spar web at $y = l/2$**

Fig. 7 Shear-stress trends under load case 1; wing with no ribs.

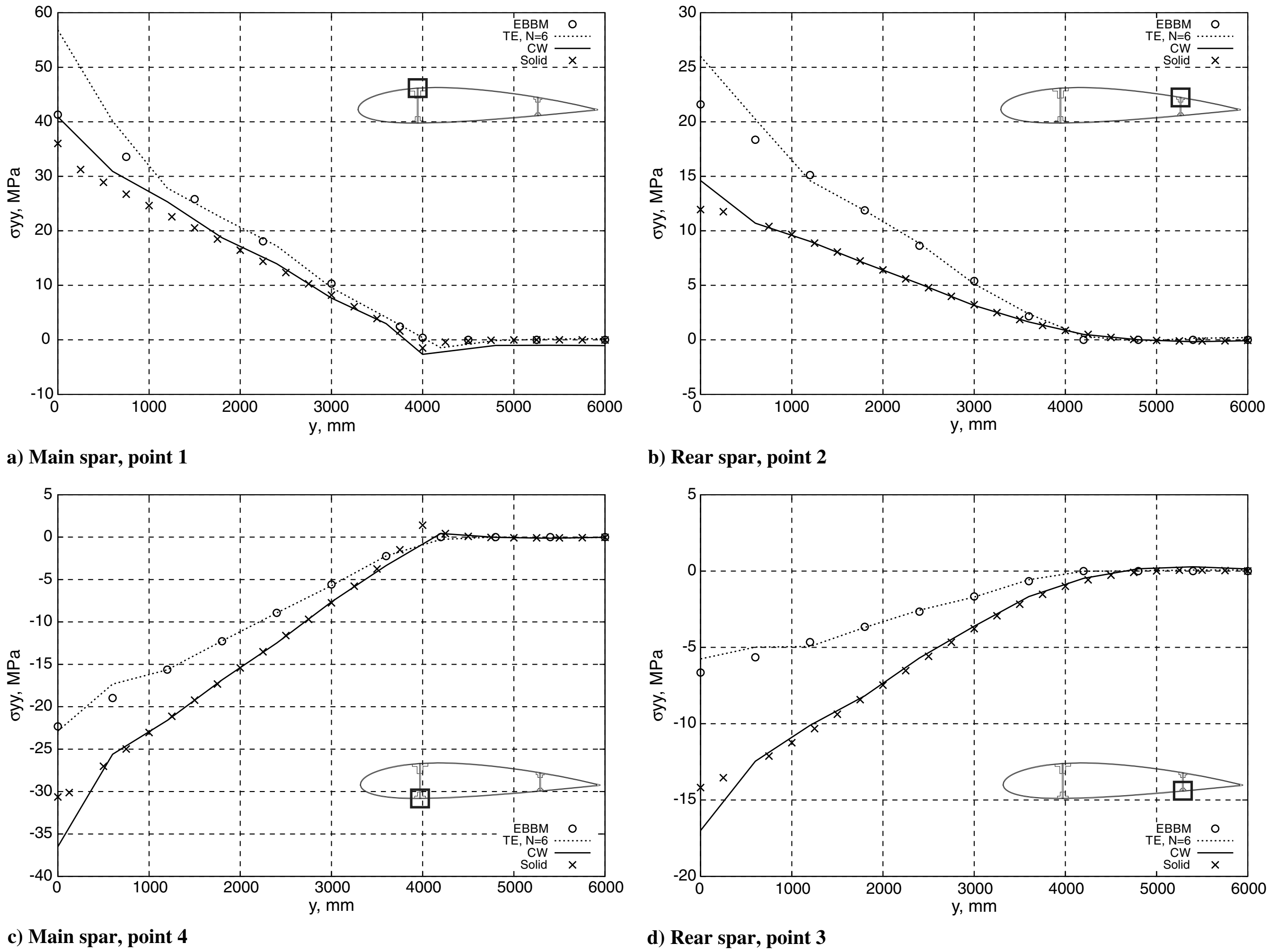

a) Main spar, point 1

b) Rear spar, point 2

c) Main spar, point 4

d) Rear spar, point 3

Fig. 8 Spanwise axial stress trends under load case 1; wing with no ribs.

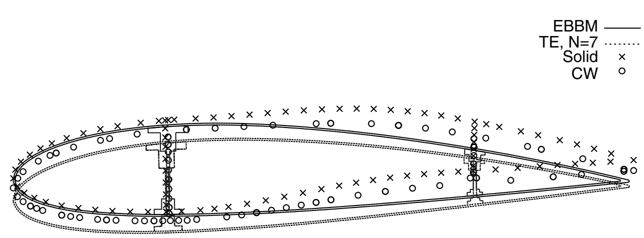

Fig. 9 Tip cross-section deformation under load case 2; wing with no ribs.

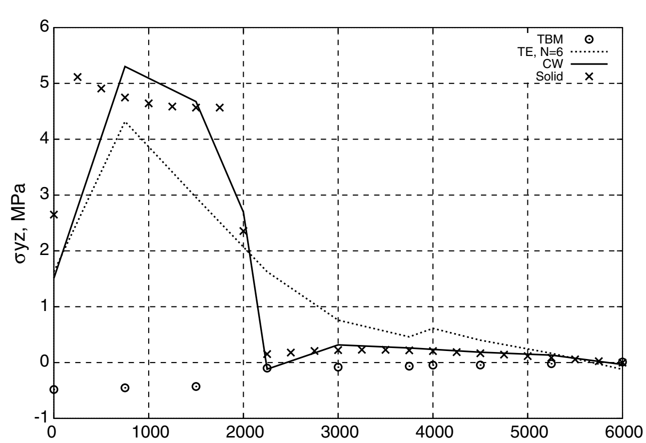

Fig. 10 Spanwise distribution of the transverse shear stress σ_{yz} at point 5 under load case 3; wing with no ribs.

1) Due to ribs, the wing is more rigid within the cross-sectional plane. As a consequence, higher-order effects play a marginal role in this particular wing configuration. For this reason, even classical beam models can be effective in detecting the structure deformation.

2) Nevertheless, stress analysis still requires refined models. If compared to the solid model, maximum relative errors close to 70% for axial stress are still produced by EBBM and TE analyses. However, results in terms of stress components are slightly improved with respect to the analysis of the rib-free configuration.

3) CW models are very effective and efficient, even in the case of wing structures with ribs.

Interesting guidelines for the development of advanced beam models including inertial effects can be extrapolated from the analysis of the ribbed three-bay wingbox with an underside window in the midbay, which is discussed hereinafter. The cross section of the midbay is shown Fig. 13 in order to better highlight the considered geometry. The structure underwent load case 2, as detailed in Table 1. Results in terms of displacements and stress components are reported in the last columns of Table 3. Figure 14 shows the distribution of the axial stress σ_{yy} along the four stringers evaluated according to different models. Finally, for the same load case, Fig. 15 summarizes the comparison of the results in terms of shear stress σ_{yz} between the CW and the Nastran 3-D models. In particular, the figure shows the spanwise distribution of the shear stress at the center of the main spar web for the wing without ribs, the ribbed wing, and the ribbed wing with the underside opening at the midbay. Some further remarks can be made:

1) The window results in concentrations of axial stress in the lower spar caps that are close to the middle bay. This phenomenon is correctly predicted by both the CW and Nastran solid models.

Table 3 Selected values of u_z, σ_{yy}, and σ_{yz}; three-bay wing, both without and with underside window, subjected to load case 2

	Three-bay wing				Three-bay wing with opening			
Models	u_z[a] mm	σ_{yy}[b] MPa	σ_{yz}[c] MPa	DOFs	u_z[a] mm	σ_{yy}[b] MPa	σ_{yz}[c] MPa	DOFs
Classical models								
EBBM	22.443	2.677	— —	84	22.897	2.532	— —	84
TBM	22.440	2.674	0.114	140	22.898	2.551	0.128	140
Higher-order models based on TE								
$N = 2$	21.502	3.027	0.087	504	22.004	2.880	0.062	504
$N = 4$	21.838	2.414	0.948	1260	22.419	2.275	1.058	1260
$N = 5$	21.925	2.591	1.113	1764	22.551	2.449	1.348	1764
$N = 6$	21.964	2.887	1.020	2352	22.640	2.733	1.337	2352
$N = 7$	22.007	3.135	0.986	3024	22.736	3.020	1.297	3024
$N = 8$	22.026	3.121	0.994	3780	22.797	3.011	1.371	3780
Higher-order model based on LE								
CW	22.214	7.873	0.779	24864	23.024	7.658	1.100	24165
MSC Nastran model								
Solid	22.456	7.958	0.726	171321	23.288	6.312	1.033	129183

[a] u_z at point 2, $y = l$.
[b] σ_{yy} at point 3, $y = 0$.
[c] σ_{yz} at point 5, $y = l/2$.

2) The shear stress in the spar webs increases as a consequence of the window. Even in this case, the 1-D CW model is the best compromise between accuracy and computational efficiency.

3) Classical and TE (even higher-order) models are not recommended for the static analysis of wing structures, especially if windows are present or accurate stress analyses are required.

B. Free Vibration Analyses

The free vibration characteristics of the metallic benchmark wing are discussed in this section. The configuration with no ribs is addressed first. Table 4 shows the first eight natural frequencies of the wing, both without and with a nonstructural mass applied. The weight of the nonstructural mass was equal to 300 kg, and it was applied as in

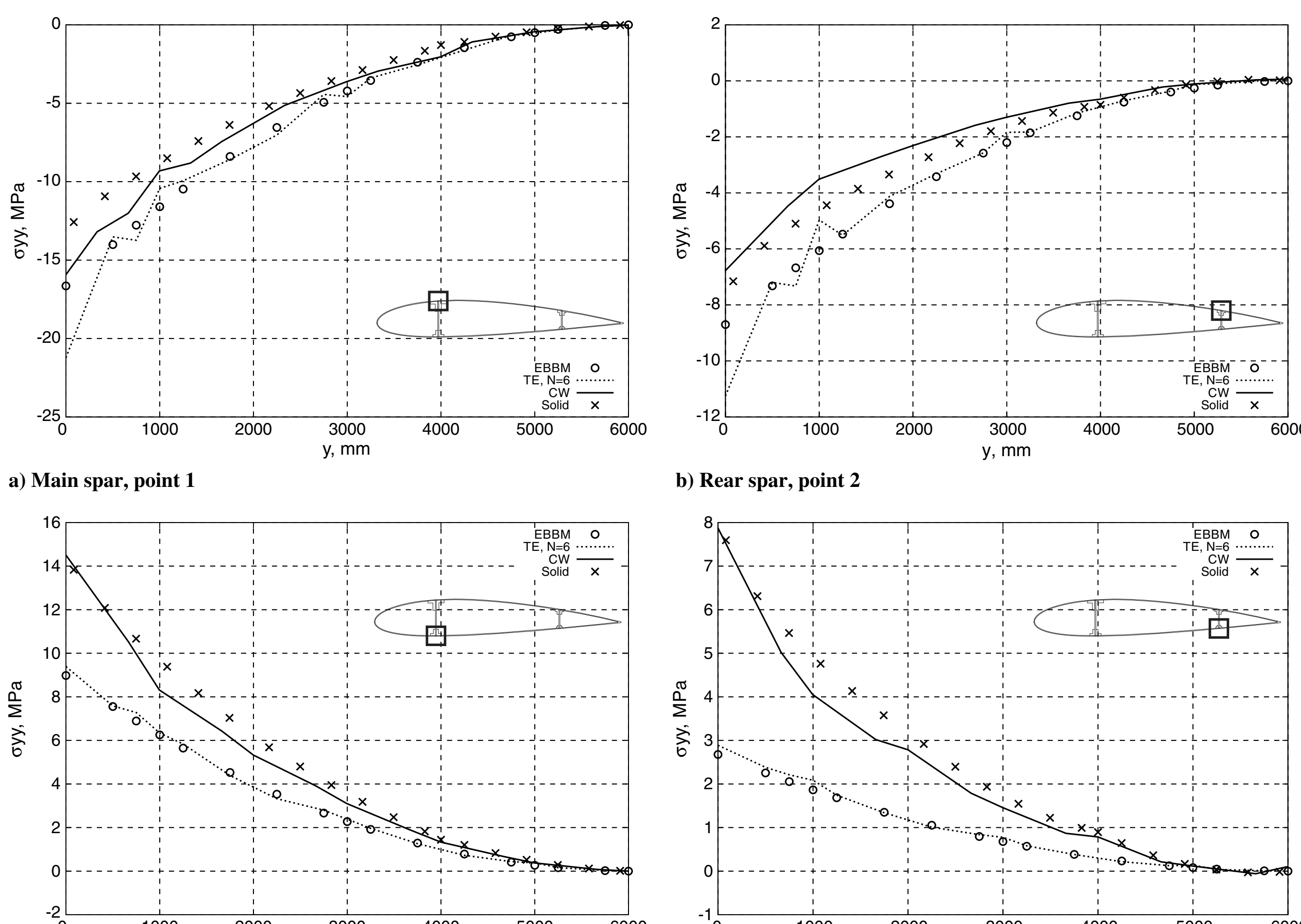

a) Main spar, point 1

b) Rear spar, point 2

c) Main spar, point 4

d) Rear spar, point 3

Fig. 11 Spanwise axial stress trends under load case 2; three-bay wing with ribs.

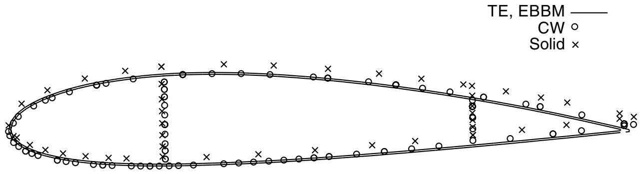

Fig. 12 Tip cross-section deformation under load case 2; three-bay wing with ribs.

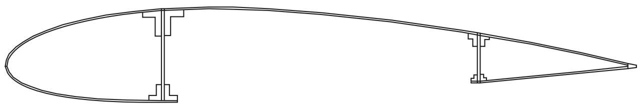

Fig. 13 Cross-section of the open midbay of the ribbed wing.

load case 3 (see Table 1). In Table 4, the results by the classical beam models (EBBM and TBM) are given in the second and third columns. The natural frequencies according to the second- ($N = 2$), fourth- ($N = 4$), sixth- ($N = 6$), and eighth-order (N = 8) refined TE beam models are given in the fourth to seventh columns. The results of the CW model are quoted in the eighth column. In the last column of Table 4, the MSC Nastran solid solution is given for comparison purposes. The number of DOFs is also given in the table for comparing the computational demand for each model. As is clear, bending, torsional, coupled bending–torsional, and shell-like modes are detected in the proposed analysis. A shell-like mode is a modal shape that involves cross-section deformation. The term "shell" is used because this kind of mode is usually foreseen by 2-D plate/shell models. In Fig. 16, the modal assurance criterion (MAC) matrix between the CW and the solid models is shown to further underline the good accuracy of the proposed methodology. MAC is, in fact, defined as a scalar representing the degree of consistency between two distinct modal vectors (see [37]) as follows:

$$\mathrm{MAC}_{ij} = \frac{|\{\phi_{A_i}\}^T\{\phi_{B_j}\}|^2}{\{\phi_{A_i}\}^T\{\phi_{A_i}\}\{\phi_{B_j}\}\{\phi_{B_j}\}^T} \tag{24}$$

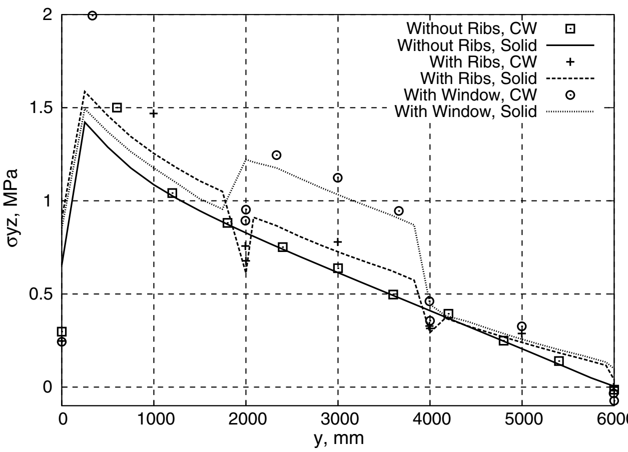

Fig. 15 Comparison of the shear stress σ_{yz} at point 5 along the spanwise direction; various configurations of the benchmark wing undergoing load case 2.

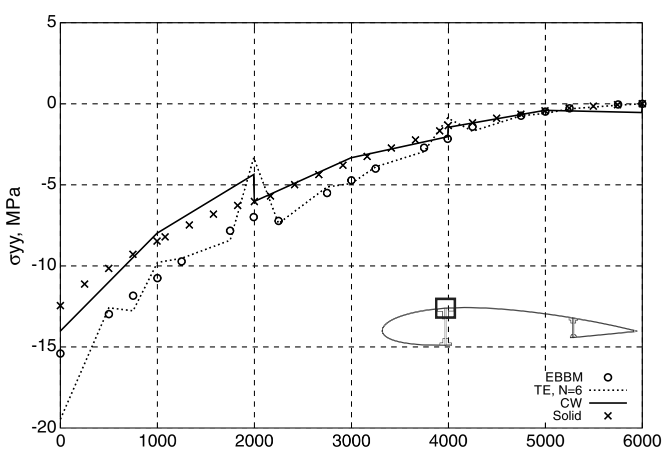

a) Main spar, point 1

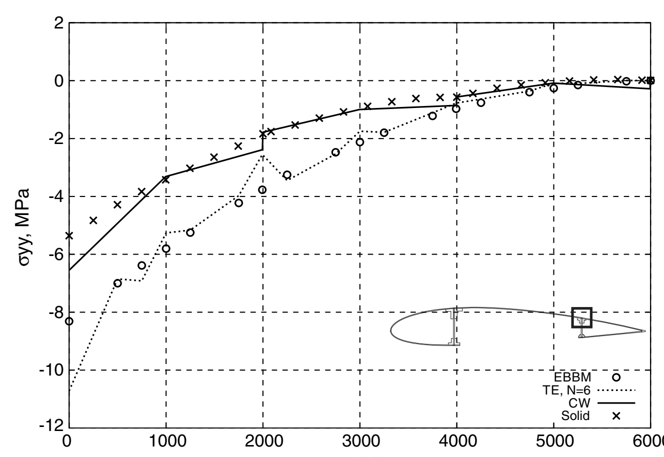

b) Rear spar, point 2

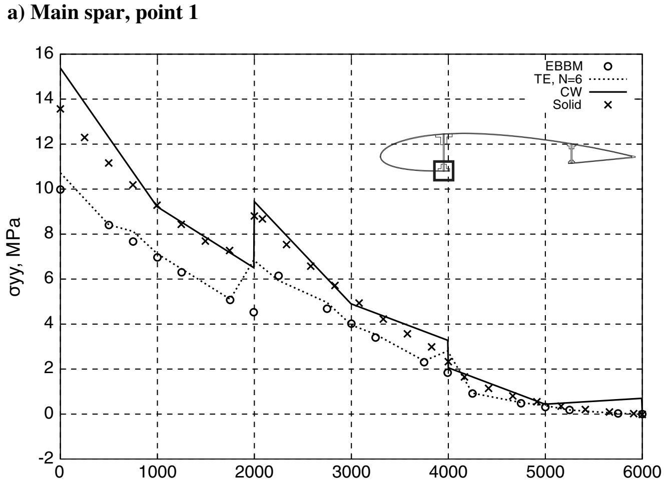

c) Main spar, point 4

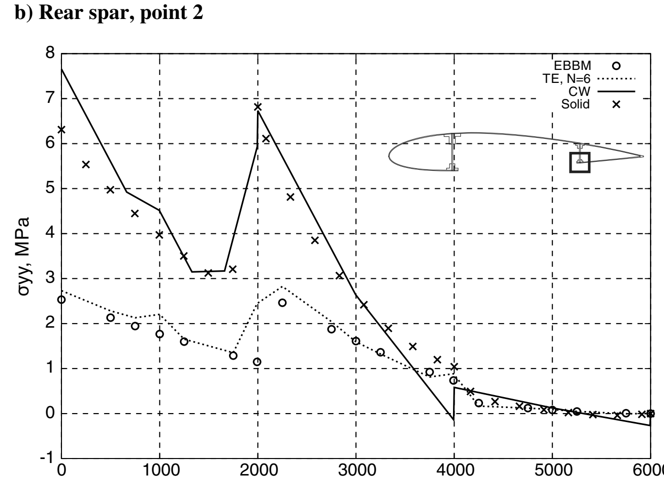

d) Rear spar, point 3

Fig. 14 Distribution of axial stress σ_{yy} along the stringers; three-bay wing with underside window subjected to load case 2.

Table 4 First 8 natural frequencies (in hertz)

	Classical and refined models based on TE						LE model	Nastran model
Mode	EBBM	TMB	$N = 2$	$N = 4$	$N = 6$	$N = 8$	CW	Solid
				Natural frequencies (in hertz)				
Bending[a]	4.22	4.22	4.29	4.26	4.25	4.24	4.23	4.21
Bending[b]	22.08	21.81	21.94	21.85	21.80	21.75	21.75	21.68
Bending[a]	26.46	26.37	26.69	26.19	26.05	25.92	25.14	24.77
Torsional	—	—	50.34	47.73	43.59	42.43	31.13	29.17
Bending[a]	73.97	73.42	74.08	71.30	70.56	69.55	59.25	56.11
Bending[a]	134.58	124.62	143.34	134.23	131.64	126.76	66.65	62.41
Shell-like	—	—	—	—	—	—	74.22	68.77
Shell-like	—	—	—	—	—	—	88.93	73.85
				Frequencies with nonstructural mass				
Bending[a]	3.82	3.81	3.88	3.84	3.83	3.82	3.82	3.80
Bending[a]	14.17	14.10	13.37	12.87	12.50	12.06	13.34	13.16
Bending[b]	19.85	19.48	19.60	19.46	19.38	19.21	19.31	19.19
Torsional	— —	— —	42.61	40.78	38.41	37.34	28.79	27.02
Coupled	— —	— —	57.74	55.12	52.39	44.38	45.10	43.14
Shell-like	— —	— —	— —	— —	— —	— —	51.92	48.96
Shell-like	— —	— —	— —	— —	— —	— —	59.35	56.65
Shell-like	— —	— —	— —	— —	— —	— —	78.20	71.45
				DOFs				
	84	140	504	1260	2352	3780	22,200	186,921

[a]Bending within *yz* plane.
[b]Bending within *xy* plane.

where $\{\phi_{A_i}\}$ is the ith eigenvector of model A, whereas $\{\phi_{B_j}\}$ is the jth eigenvector of model B. The modal assurance criterion takes on values from zero (representing no consistent correspondence) to one (representing a consistent correspondence). The case both with and without localized inertia is shown in Fig. 16. Finally, some selected modal shapes of the CW model compared with the MSC Nastran solution are shown in Fig. 17. The free vibration analyses of the rib-free configuration highlight the following:

1) Classical higher-order TE and CW models are able to detect the first bending modes.

2) Because of differential bending phenomena, which are further magnified by the nonstructural mass, higher bending frequencies are not correctly represented by classical and refined TE beam models; CW or 3-D elasticity models are needed instead.

3) At least a second-order ($N = 2$) TE model is needed to detect torsional modes. However, very high orders of expansion are necessary in the case of TE to correctly catch the related natural frequencies.

4) TE models are not able to detect shell-like frequencies. Those modes are instead correctly identified by the CW models, which are in good agreement with the Nastran models.

5) The CW model replicates the solution obtained by MSC Nastran in terms of both frequencies and modal shapes. The mean error between the two models calculated according to the first eight frequencies is, in fact, about 6%; it decreases to 4% in the case of nonstructural mass. Moreover, according to the MAC analyses, the first 19 modes are correctly described by the CW model, even though those modes do not always occupy the same positions in the eigenvector matrix with respect to the solid model. For example, modes 9 to 13 are slightly different between the CW and Nastran models if a nonstructural mass is applied because coupling phenomena occur.

The effects of the ribs on the free vibrations of the considered wing structure are further investigated, and the efficiency of the proposed

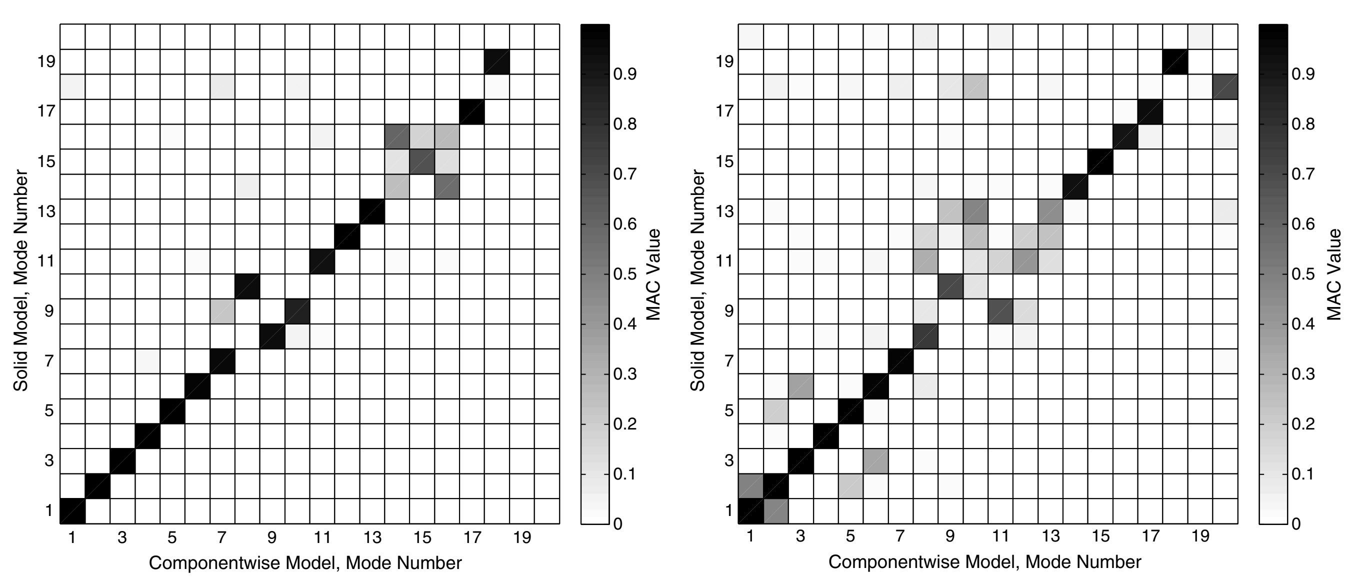

a) Without nonstructural mass **b) With nonstructural mass**

Fig. 16 MAC values between CW and MSC Nastran solid models for a wing with no ribs.

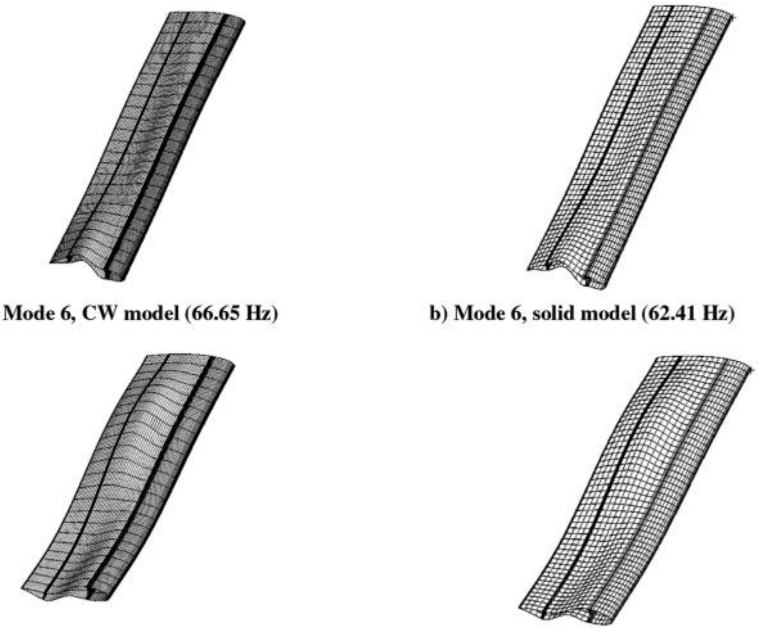

a) Mode 6, CW model (66.65 Hz)

b) Mode 6, solid model (62.41 Hz)

c) Mode 7 with nonstructural mass, CW model (59.35 Hz)

d) Mode 7 with nonstructural mass, solid model (56.65 Hz)

Fig. 17 Selected modal shapes for wing with no ribs.

1-D models are verified. Table 5 shows the first eight natural frequencies from the various models examined. The frequencies of the wing with nonstructural mass as in the previous analysis are also given in Table 5. In the study case with no localized inertia, the results by a shell/beam Abaqus model are also presented together with the results from the other models discussed so far. The correspondence between the modal shapes obtained by the MSC Nastran 3-D solid and CW models was further investigated through MAC analyses, which are shown in Fig. 18. Some selected modal shapes are finally depicted in Fig. 19. The following statements hold:

1) The overall accuracy of the proposed beam models is globally improved because of the ribs. Those transversal stiffening members, in fact, limit the cross-sectional deformation in accordance with classical beam modeling hypotheses. Thus, bending frequencies are correctly described by relatively low-order beams, such the fourth-order ($N = 4$) TE model. Classical models are still inaccurate for higher bending frequencies.

2) If localized inertia is considered, the related coupled modes need higher-order approximations in the case of TE.

3) The shell/beam Abaqus model produces some errors, even at the first bending frequencies. These errors are due to the geometrical inconsistency of the model. In fact, fictitious lines and planes are employed in the Abaqus model in order to define the domains for the 1-D and 2-D FE approximations. Thus, unlike the 3-D solid and the

Table 5 First eight natural frequencies (in hertz), wing with ribs

	Classical and refined models based on TE						LE model	Nastran and Abaqus models	
Mode	EBBM	TMB	$N = 2$	$N = 4$	$N = 6$	$N = 8$	CW	Solid	Shell/beam
Natural frequencies (in hertz)									
Bending[a]	4.12	4.12	4.18	4.14	4.15	4.15	4.14	4.12	4.43
Bending[b]	21.55	21.28	21.38	21.28	21.33	21.28	21.30	21.22	21.58
Bending[a]	25.73	25.65	25.92	25.43	25.41	25.30	25.07	24.92	26.32
Torsional	— —	— —	49.69	47.07	43.10	42.18	39.53	39.22	36.89
Bending[a]	71.50	70.96	71.56	68.90	68.53	67.90	65.29	63.87	63.40
Shell-like	— —	— —	— —	— —	— —	— —	85.85	75.01	67.73
Shell-like	— —	— —	— —	— —	— —	— —	91.70	78.60	70.49
Shell-like	— —	— —	— —	— —	— —	— —	93.65	80.43	72.74
Frequencies with nonstructural mass									
Bending[a]	3.74	3.74	3.82	3.79	3.78	3.77	3.76	3.74	— —
Bending[a]	13.98	13.91	14.15	13.84	13.74	13.67	13.56	13.51	— —
Bending[b]	19.54	19.17	19.36	19.23	19.16	19.09	19.05	18.96	— —
Torsional	— —	— —	44.03	41.88	38.95	38.20	35.66	35.38	— —
Bending[a]	51.83	51.49	55.31	53.41	52.41	51.95	50.47	50.13	— —
Coupled	— —	— —	65.44	63.35	61.73	60.59	59.18	58.73	— —
Shell-like	— —	— —	— —	— —	— —	— —	83.27	74.55	— —
Shell-like	— —	— —	— —	— —	— —	— —	87.65	76.38	— —
DOFs									
	84	140	504	1260	2352	3780	24,864	171,321	119,712

[a]Bending within yz plane.

[b]Bending within xy plane.

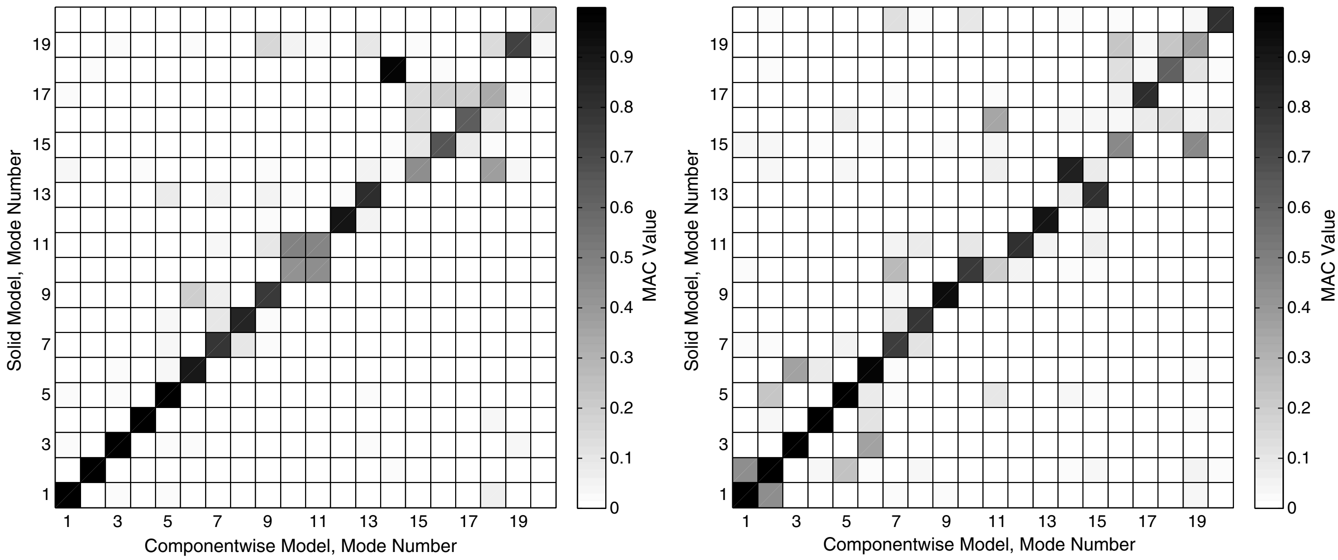

a) Without nonstructural mass **b) With nonstructural mass**

Fig. 18 MAC values between CW and MSC Nastran solid models for wing with ribs.

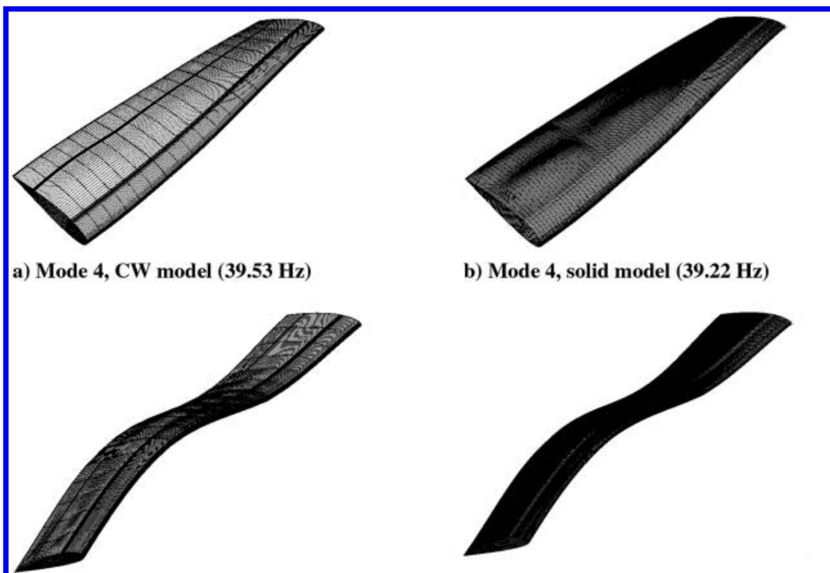

a) Mode 4, CW model (39.53 Hz) **b) Mode 4, solid model (39.22 Hz)**

c) Mode 5 with nonstructural mass, CW model (50.47 Hz) **d) Mode 5 with nonstructural mass, solid model (50.13 Hz)**

Fig. 19 Selected modal shapes for wing with ribs.

proposed beam models, a fictitious geometry is used in the shell/beam mathematical description. However, these kinds of models are widely used in common practice, and their accuracies can be, in principle, improved by exploiting experimental testing and model updating.

4) The CW approach only exploits real physical surfaces to model the structure. That was only possible up to now by using solid models.

5) The correspondence between the CW and the Nastran solid model is excellent and improved with respect to the previous analysis where ribs were not considered. As shown by the MAC, in fact, even if nonstructural masses are employed and coupled phenomena are present, the mode shapes by the CW model match those by the reference solid model.

V. Conclusions

Various finite beam elements able to include spatially distributed load factors and nonstructural masses have been formulated and applied to the analysis of metallic wing structures. The proposed models have been formulated by using the Carrera unified formulation, which is a tool for the automatic implementation of variable kinematic theories. The 3-D displacement field is, in fact, approximated through arbitrary cross-sectional functions in the framework of the 1-D Carrera unified formulation. According to previous research, refined beam models are formulated by making use of either Taylor-like or Lagrange cross-sectional approximations. The former class of polynomials results in Taylor expansion models. Classical beam theories are particular cases of the Taylor expansion (TE) linear model. If Lagrange polynomials are employed on the beam cross section, the resulting elements have only pure displacement variables, and they have been referred to as Lagrange expansion. By exploiting the natural capabilities of Lagrange expansion models to be assembled at the cross-sectional level, the componentwise approach has been formulated and discussed in this paper. The componentwise (CW) is very efficient for the analysis of multicomponent structures, such as aerospace ones, because it allows the analysts to use only the physical surfaces in the development of the mathematical model. Moreover, each component of the structure (e.g., spars, ribs, panels, etc.) is modeled by the same finite element in the framework of the CW.

In this work, particular attention has been focused on static and free vibration analysis of wing structures subjected to external inertial loads, such as load factors and nonstructural masses. The capabilities of the proposed beams have been investigated for various wing configurations, including ribbed wings, and the effects due to underside windows have been evaluated. The results have been compared to solutions from commercial finite element method (FEM) tools. In particular, both solid and shell/beam finite element (FE) models have been considered. The analyses highlight the following concluding remarks:

1) Classical beam theories cannot, of course, deal with arbitrarily distributed load factors and localized inertia. Moreover, those beam models are effective only if the deformation responses of multibay wings under bending are considered.

2) Higher-order TE models may be affected by severe errors in stress analyses, even if symmetric loading conditions and simple wing configurations are analyzed.

3) FE models built by assembling 2-D/shell and 1-D/beam elements can be affected by inconsistencies due to geometrical approximations demanded by modeling techniques.

4) CW models only use physical surfaces in modeling wing structures, and they are the best compromise in terms of accuracy and efficiency if 1) accurate stress analysis is required; 2) nonnegligible cross-sectional deformations, e.g., due to differential bending, are involved; 3) geometrical discontinuities, such as windows, are present; 4) coupling phenomena due, for example, to complex loadings, including load factors and nonstructural masses, are considered; and 5) accurate free vibration analysis involving couplings and shell-like mode shapes are needed. CW models have, in fact, been successfully compared to complex 3-D FEM models by MSC Nastran, which presented approximately one order of magnitude of degrees of freedom more.

References

[1] Kamat, M., "Effect of Shear Deformations and Rotary Inertia on Optimum Beam Frequencies," *International Journal for Numerical Methods in Engineering*, Vol. 9, No. 1, 1975, pp. 51–62. doi:10.1002/(ISSN)1097-0207

[2] Zhang, Q., and Liu, L., "Modal Analysis of Missile's Equivalent Density Finite Element Model," *Binggong Xuebao/Acta Armamentarii*, Vol. 29, No. 11, 2008, pp. 1395–1399.

[3] Ghosh, D., and Ghanem, R., "Random Eigenvalue Analysis of an Airframe," *45th AIAA/ASME/ASCE/AHS/ASC Structures, Structural Dynamics and Materials Conference*, AIAA Paper 2004-1533, 2004.

[4] Shenyan, C., "Structural Modeling and Design Optimization of Spacecraft," *Advances in the Astronautical Sciences*, Vol. 117, Dec. 2003, pp. 139–145.

[5] Nikkhoo, A., Hassanabadi, M., Azam, S., and Amiri, J., "Vibration of a Thin Rectangular Plate Subjected to Series of Moving Inertial Loads," *Mechanics Research Communications*, Vol. 55, Jan. 2014, pp. 105–113. doi:10.1016/j.mechrescom.2013.10.009

[6] Bruhn, E. F., *Analysis and Design of Flight Vehicle Structures*, Tri-State Offset Co., Cincinnati, OH, 1973.

[7] Rivello, R. M., *Theory and Analysis of Flight Structures*, McGraw–Hill, New York, 1969.

[8] Satsangi, S., and Mukhopadhyay, M., "Finite Element State Analysis of Girder Bridges Having Arbitrary Platform," *International Association for Bridge and Structural Engineering*, Vol. 17, 2006, pp. 65–94.

[9] Kolli, M., and Chandrashekhara, K., "Finite Element Analysis of Stiffened Laminated Plates Under Transverse Loading," *Composite Science and Technology*, Vol. 56, No. 12, 1996, pp. 1355–1361. doi:10.1016/S0266-3538(96)00086-3

[10] Prusty, B. G., "Linear Static Analysis of Hat Stiffened Laminated Shells Using Finite Elements," *Finite Elements in Analysis and Design*, Vol. 39, No. 12, 2003, pp. 1125–1138. doi:10.1016/S0168-874X(02)00160-9

[11] Samanta, A., and Mukhopadhyay, M., "Free Vibration Analysis of Stiffened Shells by the Finite Element Technique," *European Journal of Mechanics — A/Solids*, Vol. 23, No. 1, 2004, pp. 159–179. doi:10.1016/j.euromechsol.2003.11.001

[12] Bouabdallah, M., and Batoz, J., "Formulation and Evaluation of a Finite Element Model for the Linear Analysis of Stiffened Composite Cylindrical Panels," *Finite Elements in Analysis and Design*, Vol. 21, No. 4, 1996, pp. 265–289. doi:10.1016/0168-874X(95)00047-W

[13] Thinh, T. I., and Khoa, N. N., "Free Vibration Analysis of Stiffened Laminated Plates Using a New Stiffened Element," *Technische Mechanikl*, Vol. 28, Nos. 3–4, 2008, pp. 227–236.

[14] Vörös, G. M., "Finite Element Analysis of Stiffened Plates," *Periodica Polytechnica*, Vol. 51, No. 2, 2007, pp. 105–112. doi:10.3311/pp.me.2007-2.10

[15] Patel, S. N., Datta, P. K., and Seikh, A. H., "Buckling and Dynamic Instability Analysis of Stiffened Shell Panels," *Thin-Walled Structures*, Vol. 44, No. 4, 2006, pp. 321–333. doi:10.1016/j.tws.2006.03.004

[16] Vörös, G. M., "A Special Purpose Element for Shell-Beam Systems," *Computers and Structures*, Vol. 29, No. 2, 1988, pp. 301–308. doi:10.1016/0045-7949(88)90263-5

[17] Carrera, E., Cinefra, M., Petrolo, M., and Zappino, E., *Finite Element Analysis of Structures Through Unified Formulation*, Wiley, New York, 2014.

[18] Carrera, E., Giunta, G., and Petrolo, M., *Beam Structures: Classical and Advanced Theories*, Wiley, New York, 2011. doi:10.1002/9781119978565

[19] Carrera, E., Pagani, A., Petrolo, M., and Zappino, E., "Recent Developments on Refined Theories for Beams with Applications," *Mechanical Engineering Reviews*, Vol. 2, No. 2, 2015, Paper 14-00298, doi:10.1299/mer.14-00298

[20] Carrera, E., Pagani, A., and Zangallo, F., "Thin-Walled Beams Subjected to Load Factors and Non-Structural Masses," *International Journal of Mechanical Sciences*, Vol. 81, April 2014, pp. 109–119. doi:10.1016/j.ijmecsci.2014.02.015

[21] Pagani, A., Zangallo, F., and Carrera, E., "Influence of Non-Structural Localized Inertia on Free Vibration Response of Thin-Walled Structures by Variable Kinematic Beam Formulations," *Shock and Vibration*, Vol. 2014, April 2014, Paper 141982, doi:10.1155/2014/141982

[22] Carrera, E., Pagani, A., and Zangallo, F., "Comparison of Various 1-D, 2-D, and 3-D FE Models for the Analysis of Thin-Walled Box with Transverse Ribs Subjected to Load Factors," *Finite Elements in Analysis and Design*, Vol. 95, March 2015, pp. 1–11. doi:10.1016/j.finel.2014.10.004

[23] Novozhilov, V. V., *Theory of Elasticity*, Pergamon Press, New York, 1961.

[24] Kapania, K., and Raciti, S., "Recent Advances in Analysis of Laminated Beams and Plates, Part I: Shear Effects and Buckling," *AIAA Journal*, Vol. 27, No. 7, 1989, pp. 923–935. doi:10.2514/3.10202

[25] Kapania, K., and Raciti, S., "Recent Advances in Analysis of Laminated Beams and Plates, Part II: Vibrations and Wave Propagation," *AIAA Journal*, Vol. 27, No. 7, 1989, pp. 935–946. doi:10.2514/3.59909

[26] Washizu, K., *Variational Methods in Elasticity and Plasticity*, Pergamon, Oxford, 1968.

[27] Vlasov, V. Z., *Thin-Walled Elastic Beams*, National Science Foundation, Washington, D.C., 1961.

[28] Heyliger, P. R., and Reddy, J. N., "A Higher Order Beam Finite Element for Bending and Vibration Problems," *Journal of Sound and Vibration*, Vol. 126, No. 2, 1988, pp. 309–326. doi:10.1016/0022-460X(88)90244-1

[29] Carrera, E., and Petrolo, M., "Refined Beam Elements with only Displacement Variables and Plate/Shell Capabilities," *Meccanica*, Vol. 47, No. 3, 2012, pp. 537–556. doi:10.1007/s11012-011-9466-5

[30] Carrera, E., Pagani, A., and Petrolo, M., "Classical, Refined and Component-Wise Theories for Static Analysis of Reinforced-Shell Wing Structures," *AIAA Journal*, Vol. 51, No. 5, 2013, pp. 1255–1268. doi:10.2514/1.J052331

[31] Carrera, E., Pagani, A., and Petrolo, M., "Component-Wise Method Applied to Vibration of Wing Structures," *Journal of Applied Mechanics*, Vol. 80, No. 4, 2013, Paper 041012. doi:10.1115/1.4007849

[32] Carrera, E., Pagani, A., and Petrolo, M., "Refined 1-D Finite Elements for the Analysis of Secondary, Primary, and Complete Civil Engineering Structures," *Journal of Structural Engineering*, Vol. 141, No. 4, April 2015, Paper 04014123. doi:10.1061/(ASCE)ST.1943-541X.0001076

[33] Oñate, E., *Structural Analysis with the Finite Element Method: Linear Statics*, Vol. 1, Springer, New York, 2009.

[34] Carrera, E., Pagani, A., and Petrolo, M., "Use of Lagrange Multipliers to Combine 1-D Variable Kinematic Finite Elements," *Computers and Structures*, Vol. 129, Dec. 2013, pp. 194–206. doi:10.1016/j.compstruc.2013.07.005

[35] Carrera, E., and Pagani, A., "Analysis of Reinforced and Thin-walled Structures by Multi-Line Refined 1-D/Beam Models," *International Journal of Mechanical Sciences*, Vol. 75, Oct. 2013, pp. 278–287. doi:10.1016/j.ijmecsci.2013.07.010

[36] Bathe, K., *Finite Element Procedure*, Prentice–Hall, Upper Saddle River, NJ, 1996.

[37] Allemang, R. J., and Brown, D. L., "A Correlation Coefficient for Modal Vector Analysis," *Proceedings of the International Modal Analysis Conference*, Orlando, FL, 1982, pp. 110–116.

R. Kapania
Associate Editor